A Study on Intelligent Optical Bone Densitometry

TAKHELLAMBAM GAUTAM MEITEI[1], WEI-CHUN CHANG[1,2], POU-LENG CHEONG[1,3,4], YI-MIN WANG[1], AND CHIA-WEI SUN [1,5,6]

[1]Department of Photonics, College of Electrical and Computer Engineering, National Yang Ming Chiao Tung University, Hsinchu 30010, Taiwan
[2]Department of Orthopedic Surgery, Wan Fang Hospital, Taipei Medical University, Taipei 110, Taiwan
[3]Department of Biological Science and Technology, National Yang Ming Chiao Tung University, Hsinchu 30010, Taiwan
[4]Department of Pediatrics, National Taiwan University Hospital Hsinchu Branch, Hsinchu 300, Taiwan
[5]Institute of Biomedical Engineering, College of Electrical and Computer Engineering, National Yang Ming Chiao Tung University, Hsinchu 30010, Taiwan
[6]Medical Device Innovation and Translation Center, National Yang Ming Chiao Tung University, Taipei City 112, Taiwan

CORRESPONDING AUTHOR: C.-W. SUN (chiaweisun@nycu.edu.tw)

ABSTRACT   Osteoporosis is a prevalent chronic disease worldwide, particularly affecting the aging population. The gold standard diagnostic tool for osteoporosis is Dual-energy X-ray Absorptiometry (DXA). However, the expensive cost of the DXA machine and the need for skilled professionals to operate it restrict its accessibility to the general public. This paper builds upon previous research and proposes a novel approach for rapidly screening bone density. The method involves utilizing near-infrared light to capture local body information within the human body. Deep learning techniques are employed to analyze the obtained data and extract meaningful insights related to bone density. Our initial prediction, utilizing multi-linear regression, demonstrated a strong correlation ($r = 0.98$, p-value $= 0.003**$) with the measured Bone Mineral Density (BMD) obtained from Dual-energy X-ray Absorptiometry (DXA). This indicates a highly significant relationship between the predicted values and the actual BMD measurements. A deep learning-based algorithm is applied to analyze the underlying information further to predict bone density at the wrist, hip, and spine. The prediction of bone densities in the hip and spine holds significant importance due to their status as gold-standard sites for assessing an individual's bone density. Our prediction rate had an error margin below 10% for the wrist and below 20% for the hip and spine bone density.

INDEX TERMS   Bone mineral density, deep learning, multi-linear regression, near infrared imaging, osteoporosis, osteoporosis screening device.

I. INTRODUCTION

THE skeletal structure in our bodies serves as a foundational framework that provides support from birth onwards. It undergoes a transformative process and reaches its peak bone mass during our mid-twenties. However, as we age, this bone mass gradually declines, and women, in particular, experience accelerated loss after menopause. Unfortunately, chronic diseases like osteoporosis often go unnoticed as they do not present observable symptoms, despite the general awareness surrounding various other chronic conditions. Osteoporosis, characterized by weakened bones and an elevated risk of fractures, has emerged as a significant global health concern. Its impact on morbidity and mortality is widely acknowledged by the World Health Organization (WHO). The consequences of osteoporotic fractures, both in terms of individual health outcomes and healthcare burden, underscore the importance of addressing this condition as a priority in public health initiatives [1]. Fragility fractures, also referred to as minimally traumatic fractures, commonly occur in the hip, spine, and wrist, typically resulting from falls while standing. These fractures are a significant clinical consequence of osteoporosis, as highlighted by the International Osteoporosis Foundation (IOF) in 2019. It emphasizes that the occurrence of fragility fractures is directly associated with the presence of osteoporosis and underscores the importance of preventing and managing this condition to reduce the incidence of such fractures [2]. Osteoporosis has not only emerged as a significant health

issue but also as an economic concern, imposing substantial burdens not only on the affected individuals but also on their families. The financial impact associated with osteoporosis includes the costs of medical treatments, hospitalizations, rehabilitation, and long-term care. Additionally, indirect costs arise from lost productivity and income due to reduced work capacity or disability resulting from osteoporotic fractures. These economic burdens highlight the need for effective prevention, early detection, and management strategies to mitigate the financial consequences of osteoporosis on both patients and their families [3]. Osteoporosis can be effectively managed through prompt anti-osteoporosis therapy, which plays a crucial role in reducing the risks associated with osteoporotic fractures. By identifying the condition at an early stage and implementing appropriate interventions, such as lifestyle modifications, medication, and regular monitoring, individuals can minimize the impact of osteoporosis and reduce the likelihood of experiencing related complications [4]. Diagnosis of osteoporosis can be based on the clinical history of low traumatic fracture or based on their bone mineral density (BMD) T-score. The gold standard measurement of BMD is based on Dual-energy X-ray Absorptiometry (DXA) [5]. Per the official positions of the International Society for Clinical Densitometry (ISCD) for adults, the assessment of bone density should involve the measurement of either the lumbar spine or the hip bones. If none of them can be measured, the measurement at 1/3 of the radius of the lateral forearm can be used instead [6]. The diagnostic criteria established by the WHO based on the fracture rate of white postmenopausal women and referring to the ISCD and national guidelines when the bone mineral density is less than or equal to 2.5 standard deviations compared with the average bone mineral density of white women aged 20 to 29 (T-score ≤ -2.5) will be defined as osteoporosis or severe osteoporosis and less than 1 to 2.5 standard deviations ($-2.5 <$ T-score < -1) will be defined as osteopenia or low bone mass and the rest is defined as normal bone [7]. Various diagnosis methods include Dual photon absorptiometry (DPA) [8], Quantitative Computed Tomography (QCT) [9], [10], Quantitative Ultrasonography (QUS) [11], and Dual X-ray absorptiometry (DXA) [12]. While QCT may offer higher precision in measuring bone density, DXA remains the primary choice for routine clinical use due to its established clinical guidelines, extensive research validation, and widespread availability [13]. Nevertheless, there are several inherent limitations associated with DXA. These encompass the considerable expenses involved in its construction, longer scan duration, and the need for skilled professionals to operate the equipment. Consequently, these factors pose challenges to the widespread accessibility of DXA, making it less feasible for the general population to avail themselves of its benefits conveniently and ubiquitously. Compared to DXA, QCT offers the advantage of accurately measuring mineral density in distinct cortical bone and trabecular regions of interest. However, it shares similar limitations

with DXA [14]. On the other hand, the QUS system provides a relatively radiation-free assessment of bone mass. Nevertheless, it falls short of providing precise information about bone physiological status, thus limiting its clinical applications [15].

In theory, diffuse optics tomography utilizing near-infrared light offers several advantages, including its non-radiative and non-invasive nature, real-time analysis capabilities, and cost-effectiveness. Given the complexity of the human body as a medium, it is crucial to consider the optical window of biological tissue. Specifically, wavelengths ranging from 750nm to 950nm are preferred in the study as they are less influenced by the presence of fat and collagen, enabling the acquisition of more comprehensive tissue information [16]. The scattering coefficient, μs (10 cm-1) in our body, is usually larger than the absorption coefficient, μa (0.1 cm-1), and hence the light signal obtained is mostly diffused photons [17]. Takeuchi et al. presented a time-resolved spectroscopy system using a Near-Infrared laser to study the penetration of light on human bone and concluded that the scattering characteristics of light from the bone strongly correlated to the BMD [18]. In a study conducted by Chung et al., the researchers examined the association between optical attenuation measured from the distal radius using Near Infra-red (NIR) light and BMD assessed by DXA. The findings of their investigation revealed a robust correlation between the optical attenuation values and BMD measurements. This suggests that the NIR-based optical attenuation technique has the potential to serve as a valuable indicator of bone density, as assessed by DXA [19].

The widespread adoption of Machine Learning (ML) in recent times has made it pervasive across various domains, including advanced technologies like mobile phones and robotics, as well as critical sectors such as healthcare. ML has emerged as a valuable tool in disease diagnosis, offering improved safety measures. By utilizing ML algorithms and techniques, healthcare professionals can effectively analyze extensive medical data, encompassing patient records and imaging scans, thereby facilitating precise disease diagnosis. The integration of ML in healthcare empowers medical practitioners to make informed decisions and enhance patient care [20]. By combining ML algorithms, it becomes feasible to develop a streamlined and efficient diagnostic system that can accurately identify osteoporosis. Such a tool would offer the advantage of being readily available to the general population, simplifying the screening process and potentially enabling earlier detection of osteoporosis.

The fundamental premise of this study is that increased bone density results in reduced light transmission through the bone structure. In line with this concept, we employed ML techniques to analyze wrist images captured using near-infrared LEDs. In our initial investigation, we assessed the practicality of employing real-time near-infrared optical bone densitometry (OBD) for measuring the ultra-distal radius of a subject. This involved illuminating the area with near-infrared

light and utilizing a simple setup consisting of NIR-LEDs and a CMOS camera. Subsequently, we employed multi-linear regression (MLR) to predict the bone density of the subject based on the gathered data. This preliminary analysis aimed to evaluate the feasibility of using this approach as a potential tool for non-invasive bone density assessment. Following the successful feasibility test, our subsequent step involved the development of a portable near-infrared light bone densitometry optical system. This system was designed to examine the intensity of diffused photons using image processing techniques complemented by deep learning algorithms. We aimed to employ an integrated approach to predict bone density at different body parts (wrist, hip, and spine), referring to the guidelines set by the ISCD, as it holds substantial value in the field of bone health assessment. This system offers unique advantages, including real-time capability, non-invasiveness, cost-effectiveness, and portability.

By combining advanced imaging technologies with deep learning methodologies, we aimed to enhance the accuracy and efficiency of bone density prediction in a portable and accessible manner. Our intention is not to replace DXA with our device but rather to complement its capabilities and address certain limitations by extending its reach. We aspire to develop our device as a rapid screening tool suitable for outpatient or home use. Given the non-radiative and non-invasive nature of near-infrared technology, it does not possess the same depth of penetration as X-rays. Therefore, we chose to collect near-infrared images from the distal radius and ulna of both the left and right hand to predict bone density in the wrist, spine, and hip. Accurate prediction of bone densities at the wrist, hip, and spine holds significant implications for clinicians, researchers, and patients alike. This knowledge enables healthcare professionals to provide targeted interventions and implement appropriate measures to mitigate the risks associated with bone-related conditions. Additionally, patients can gain a deeper understanding of their bone health, enabling them to actively participate in their care and take proactive steps toward maintaining optimal bone strength and reducing fracture risks.

II. EXPERIMENTAL METHODS
A. STUDY DESIGN AND PARTICIPATION ENROLMENT
Before the commencement of the study, all participants were provided with a consent form (NCTU-REC-105-041) approved by the Research Ethics Committee for Human Subject Protection. The study was conducted in collaboration with Taipei Wan Fang Hospital, Taiwan, and a total of 68 participants were recruited. This group comprised 12 males and 56 females, with an average age of 56.4 ± 20 years. Adherence to ethical guidelines and obtaining informed consent from the participants ensured the protection of human subjects throughout the entire research process. A subset of the total data, consisting of 11 subjects (7 males and 4 females), was initially obtained for the preliminary test using the multi-linear regression (MLR) method.

The remaining data, comprising 57 subjects (5 males and 52 females), was utilized to develop our deep learning model. Within this dataset, 90% of the data was allocated for training purposes, while the remaining 10% was designated as testing data. In our research, we acknowledge that the sample displays a bias toward a particular demographic, raising concerns about the generalizability of our findings beyond the studied population. To mitigate this concern in future studies, we recommend implementing targeted recruitment strategies to ensure a more diverse participant pool encompassing a wider range of demographics.

For each subject, bone density data at the wrist, hip, and spine were acquired using DXA, which will serve as the reference standard. Additionally, wrist images were captured using our custom-designed prototype under near-infrared light. These wrist images, along with the corresponding DXA measurements, were utilized for the analysis and development of our proposed method for bone density prediction. By combining DXA data with the near-infrared images, we aimed to enhance the accuracy and reliability of our predictive model for assessing bone density at different anatomical sites.

B. SYSTEM HARDWARE
In our study, we utilized three types of aluminum gallium arsenide (AlGaAs) LEDs with wavelengths of 770nm, 850nm, and 940nm as the light source for illuminating the subjects' wrists. To capture the near-infrared images, we employed a high-performance and high-sensitivity small industrial CMOS camera, specifically the UI-1250LE-M-GL model developed by German Imaging Development Systems (IDS). The rationale behind this choice was rooted in its high sensitivity. However, it is essential to recognize the potential benefits of exploring alternative hardware configurations for future studies. Additionally, we integrated a 6mm UC series 33-301 fixed focal length lens from Edmund Optics into the camera setup, providing a field of vision (FOV) of approximately 58.9 degrees. The DXA system utilized in this study is the Prodigy DXA system, which is manufactured by GE-Lunar and based in Madison, Wisconsin.

C. MULTI-LINEAR REGRESSION ANALYSIS
To conduct the multi-linear regression (MLR) analysis, a simple setup was devised to capture the wrist images, as illustrated in Fig. 1(a). The CMOS camera was positioned on a custom-made 3D-printed stand, while the LEDs were positioned at the base of the stand. The LEDs were arranged in an array configuration and could be individually turned on and off as required for the imaging process. The distance between the light source and the camera is kept at about 8cm. Wrist images of the 11 subjects are obtained for each around the lister tubercle. For each subject, a total of 13 parameters were selected from the bone image and the subject's physiological data.

The parameters extracted from the wrist images encompass various aspects. They include the average intensity of the
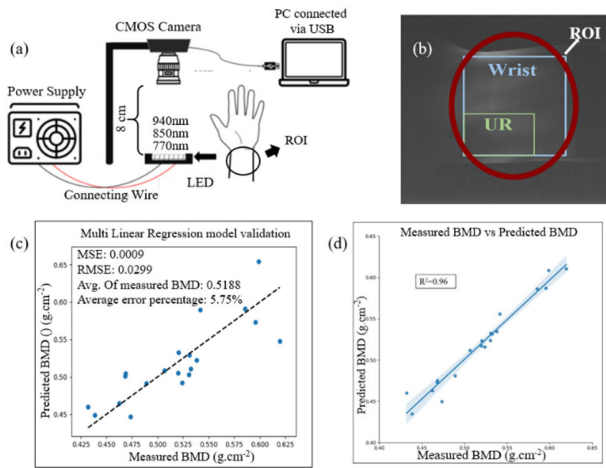
FIGURE 1. (a) The near-infrared-based bone densitometry system setup for the preliminary analysis. (b) Wrist image of a subject's right hand under 850nm with their respective ROI. (UR – Ultra-Distal Radius) (c) 10-fold Model validation. (MSE: Mean Square Error, RMSE: Root Mean Square Error) (d) Prediction Performance (R^2 = 0.96).

entire wrist area under each wavelength (770nm, 850nm, and 940nm), the average intensity specifically at the ultra-distal radius for each wavelength, and the ratio between the average intensity of the wrist and the ultra-distal radius for each wavelength. This results in a total of nine image parameters, with three parameters corresponding to each wavelength. Additionally, the physiological parameters considered in the analysis are the width, thickness, and circumference of the wrist, along with the sex of each subject. These four physiological parameters are essential to capture the individual characteristics of the subjects. In total, these 13 parameters, comprising nine image parameters and four physiological parameters, are utilized as independent variables in our multi-linear regression model.

For each subject, the DXA bone mineral density (BMD) measurements at the bilateral distal radius were obtained and recorded. These measurements were stored for comparison and further analysis. Out of the 11 recorded data, 10 of them were used to build our multi-linear regression model, while one subject's data was held out as test data. Using the 13 parameters derived from the wrist images and the subject's physiological data, we recalculated the BMD values for the 10 subjects in our model. The purpose of this step was to evaluate the performance and accuracy of our model. The recalculated BMD values were then compared to the BMD measurements obtained via DXA. The analysis revealed a strong correlation between the recalculated BMD and the DXA-measured BMD, with a correlation coefficient (r) of 0.98. The coefficient of determination (R2) was found to be 0.96, indicating that 96% of the variance in BMD could be explained by our model. Furthermore, the p-value, which was approximately 0.003∗∗, indicated that the observed correlation was statistically significant at a significance level of 0.05. These findings suggest that our multi-linear regression model, based on the 13 parameters,

is highly accurate in predicting BMD and effectively captures the relationship between the selected parameters and the actual BMD measurements obtained via DXA.

To further validate the performance of our model, we employed a K-fold cross-validation method. Using a 10-fold cross-validation approach, we evaluated the predicted BMD values against the measured BMD values. The results of cross-validation showed that the majority of the predicted BMD values were in close agreement with the measured BMD values, as depicted in Fig.1(c). However, a few data points exhibited relatively larger differences between the predicted and measured BMD values. To quantify the overall accuracy of our model, we calculated the root mean square error (RMSE) as an indicator. The RMSE value was approximately 0.0299, indicating that, on average, the predicted BMD values had an error of about ± 0.0299 g/cm2 compared to the measured BMD values. This suggests that our model has a relatively small average prediction error for BMD measurements.

To assess the performance of our model on an osteoporosis patient, we tested it on a 70-year-old female patient. The relative error of our model was approximately 2.1% for the left wrist BMD (DXA-BMD: 0.317, predicted BMD: 0.323) and 4.4% for the right wrist BMD (DXA-BMD: 0.305, predicted BMD: 0.291). These results indicate that our model is capable of providing reasonably accurate predictions for BMD values in real-world scenarios. Additionally, we observed a negative correlation between the optical parameters and BMD. This finding aligns with expectations, as higher bone density typically leads to reduced penetration of light through the bone. Therefore, the observed negative correlation reinforces the practicality of our model in capturing the relationship between optical parameters and BMD, supporting its reliability in predicting bone density.

D. PORTABLE NEAR-INFRARED LIGHT BONE DENSITOMETRY

The hardware design of our optical bone densitometer has been developed with simplicity and user-friendliness in mind. The measurement site is specifically selected around the distal radius, and this region of interest (ROI) is chosen strategically. The rationale behind selecting the distal radius and ulna as the ROI is that they have relatively lower tissue thickness compared to other areas, facilitating easier penetration of light to reach the bone region. By focusing on the distal radius and ulna, which contain less tissue interference, we can enhance the accuracy and reliability of our measurements. To create an LED matrix, the LEDs are arranged in a symmetrical configuration, as depicted in Fig. 2(a). The LEDs are divided into three channels, with each channel dedicated to controlling a specific wavelength. The channels are independently controlled using pulse width modulation (PWM) through a remote. Fig. 2(b) illustrates the placement of the CMOS camera with the LED array. In this setup, the light source is positioned above the distal radius, while the sensor (CMOS camera) is positioned below it.
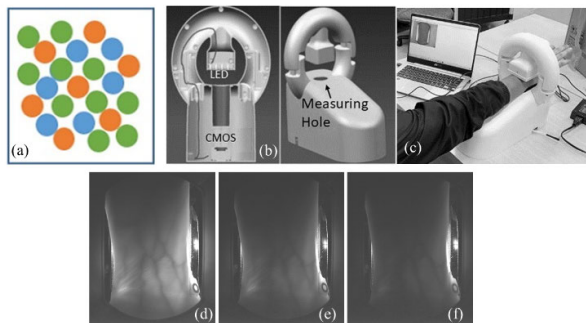
FIGURE 2. (a) Three single-wavelength LED arrangements. The orange, blue, and green represent 770nm, 850nm, and 940nm respectively (b) The OBD system with the measuring hole and the cross-section of the OBD system with the relative position of the CMOS camera and the LED matrix inside. (c) OBD measurement position and the raw images of Left wrist at (d) 770nm (e) 850nm (f) 940nm.

wrist at (d) 770nm (e) 850nm (f) 940nm

FIGURE 3. Block diagram for the bone density prediction.

The distal radius is properly aligned with the measuring hole to ensure accurate and consistent measurements. To capture data at specific wavelengths, the corresponding LED channel is selected by turning on the appropriate channel (770nm, 850nm, or 940nm). The near-infrared light emitted from the LEDs passes through the distal radius and is detected by the CMOS camera beneath it. To ensure accurate measurements and minimize interference from external light sources, the entire system is covered with a black cloth. This helps create a controlled environment for capturing wrist images under near-infrared light. For each participant, data is recorded twice for each wavelength channel, resulting in a total of 12 data points per participant. A light shield is employed to control the exposure area of the wrist during measurements. The shield has a rectangular ellipse shape with a hole measuring 6cm in length and 3cm in width. This configuration allows for precise control over the area of the wrist that is exposed to near-infrared light, ensuring consistent and reliable measurements. The distance between the light source and the camera is maintained at 8cm, providing an optimal setup for capturing wrist images with the desired field of view. This distance is carefully chosen to achieve optimal image quality and ensure accurate data collection. Fig. 2(c) depicts the measurement process using our device, showcasing the placement of the wrist, the positioning of the light source, and the CMOS camera. The raw images obtained by the CMOS camera for all three wavelengths of the left wrist are shown in Fig. 2(d-f), respectively. In addition to the optical measurements, various physiological data i.e., the participant's gender (male/female), age, wrist thickness and circumference of the wrist, menopause status (yes/no/not applicable), and wrist-fracture history, are recorded for each participant to provide comprehensive information.

In our study, we have implemented a data processing pipeline consisting of four key steps: Wrist Extraction, Histogram Equalization, Distal Radius extraction, and embedding of the previously recorded Physiological data as
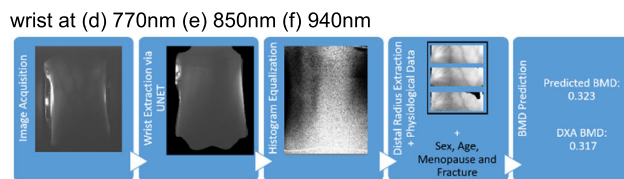
shown in Fig. 3. To facilitate these tasks, we have utilized U-Net, a deep learning network based on Convolutional Neural Networks (CNNs). The purpose of employing U-Net in our study is to perform feature extraction and image segmentation on the acquired raw wrist images. U-Net was specifically chosen for its demonstrated success in architectural design and pixel-based image segmentation tasks, particularly when dealing with limited datasets [21]. To extract the wrist information from the images, we employed a data labeling code called LabelMe to annotate the datasets. Subsequently, we trained our model using a smaller learning rate (LR = 0.0001) and utilized the Dice Loss as the loss function. The network weights were then updated using the Adam optimization algorithm. This approach allowed us to fine-tune the model and optimize its performance in accurately segmenting and extracting the wrist region from the images.

The training dataset for our study comprised 47 images used for training the U-Net model, while 11 additional images were used for verification purposes. During the training process, the U-Net model learned to output a wrist mask, which was then multiplied with the original wrist image to obtain the extracted wrist image. This approach ensured that the U-Net model effectively identified and delineated the wrist region of interest (ROI) in the images. To validate the accuracy of the selected ROI, we conducted further experiments. For several randomly chosen participants, we securely fastened their wrists with wire to the position of the Styloid Process, a bony landmark in the distal radius. Subsequently, X-ray images were taken to confirm the precise location of the distal radius. After extracting the wrist images, we further enhanced the image details by applying histogram equalization. This step was performed to enhance the visibility of image characteristics, as bone density images tend to exhibit concentrated pixel values. The histogram equalization process was applied to the extracted wrist images of the selected participants. To visualize and analyze the bone density distribution, the histogram equalized images were converted into heat maps. These heat maps were then cropped to the region of interest (ROI), corresponding to the distal radius. The heat maps were superimposed on the corresponding X-ray images, as depicted in Fig. 4(a). In the superimposed images, the color intensity represents the amount of light absorption in the area. The areas with a higher probability of being the distal radius exhibit a redder color, indicating greater photon absorption in those regions. The red box in the images denotes the region of interest (ROI) selected for the study, specifically the distal radius. It is important to note that the
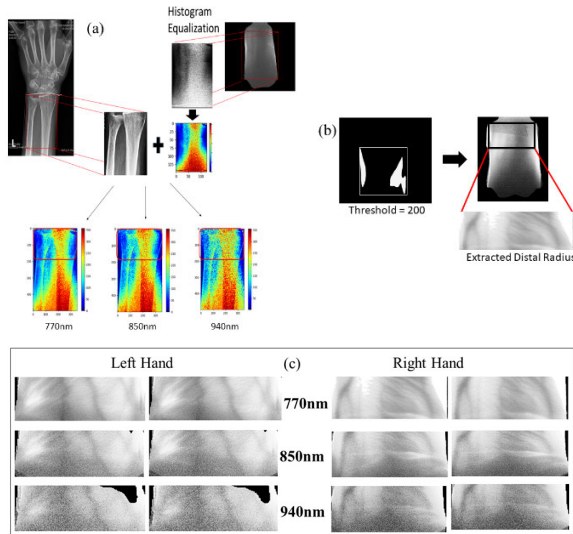
FIGURE 4. (a) The superimposition of the cropped heat map of the histogram equalized images to the cropped X-ray image of a particular participant for all three wavelengths. The red rectangular box marked in the figure shows the distal radius of the participant. (b) The selected distal radius part through the binarized image frame after thresholding. (c) The extracted 12 distal radius images of a single subject for the bone density prediction.

FIGURE 5. Bone density prediction model.

redness observed outside the red box is primarily attributed to noise originating from soft tissues such as muscles or fats. In this study, these regions of noise were disregarded and not considered for further analysis. By observing the red area within the red box, which aligns with the expected location of the distal radius, we can confirm that the selected ROI corresponds to the distal radius. This confirmation provides confidence that the subsequent analyses and measurements are focused on the intended anatomical region of interest. To ensure that only the distal radius region is considered for feature extraction and analysis, an algorithm was developed in the study. This algorithm individually marks the location of the distal radius in each participant's equalized image. A threshold value of 200 is applied to the equalized image, resulting in a two-stratified image where the distal radius region is highlighted. Using the binarized image frame, the selected distal radius portion is extracted from the previously obtained wrist image from U-net.

Consequently, for each participant, a total of 12 images of the distal radius are obtained - 6 from the left hand and 6 from the right hand, with 2 images corresponding to each wavelength. These extracted distal radius images, as illustrated in Fig. 4(c), serve as the input images for further analysis and processing in our study. To incorporate both the extracted distal radius images and the recorded physiological data, a mixed input model is designed in this study. This model is capable of handling different types of data, including image data, numerical values, and categorical data. The extracted distal radius images, as shown in Fig. 4(c), are treated as image data and form one part of the input. The physiological data, such as age, gender, fracture history, and menopause status, are considered numerical and categorical data.
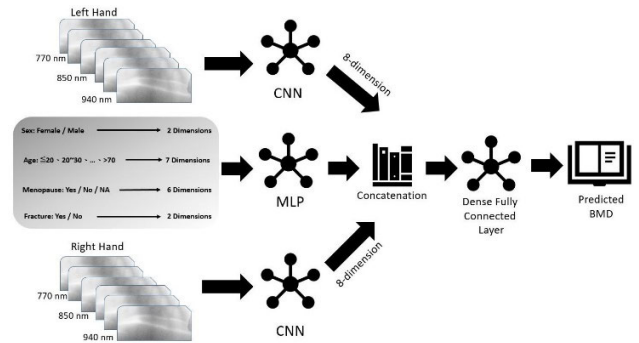
In our model architecture designed for predicting bone mineral density (BMD), we not only prioritize accuracy but also emphasize explainability for enhanced clinical transparency. To achieve this, we incorporate physiological data and distal radius images in a systematic manner. The process begins with the transformation of physiological data into a high-dimensional vector using one-hot encoding, resulting in a 17-dimensional representation. Simultaneously, distal radius images are uniformly resized to (128, 256) dimensions to ensure consistent and efficient processing. These resized images, captured at three distinct wavelengths (770nm, 850nm, and 940nm), are superimposed to construct a composite input image with dimensions (128, 256, 6 channels). Through a 6-layer convolutional layer, relevant features are extracted, transforming the images into an 8-dimensional vector representation. The subsequent step involves concatenating the 8-dimensional vectors derived from physiological data and image processing into a single, comprehensive vector. This concatenated vector undergoes further processing through a 3-layer fully connected layer, offering a compact yet interpretable representation of the combined information. The final output, a single value, serves as the predicted bone mineral density (BMD) for the participant.

To extend the capabilities of the deep learning model to predict bone density at the spine and hip, an additional image channel is introduced. The Hip and Spine model incorporates two image input channels, each corresponding to the left and right hands, along with the existing physiological data channel. By adding this extra image channel, the model becomes capable of processing and extracting features from the wrist images to the spine and hip bone density. This expanded model architecture enables the prediction of bone density at multiple locations, providing a more comprehensive assessment of bone health. The overall structure of the Hip and Spine model is depicted in Fig. 5, illustrating the integration of the additional image channel alongside the physiological data channel for accurate predictions. In this study, a total of 20 bone density prediction models are trained to cover various anatomical positions, as seen in Fig. 6. These models are trained separately for each position and both the left and right hand. For the wrist, the models are trained using the following positions: distal radius, distal ulna, 33% of the distal radius,
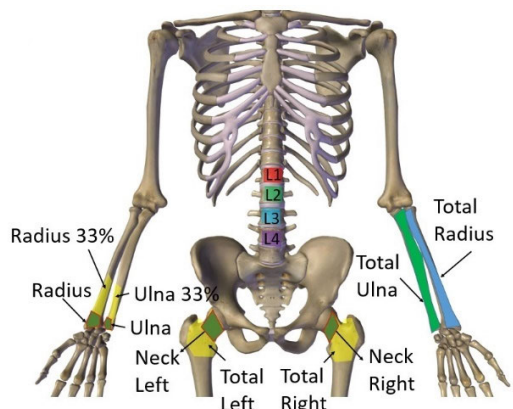
FIGURE 6. Bone density prediction positions.

33% of the distal ulna, total radius, and total ulna. Each position is entered into the model separately, depending on whether the optical bone densitometer (OBD) distal radius image used is from the left or right hand. For the spine and hip, the positions include L1, L2, L3, and L4 of the spine, as well as the left and right hip bone neck, and total left and total right hip bone. In the case of the spine and hip predictions, both the left and right distal radius images are used together as input data.

By training models for these various positions, the study aims to provide comprehensive predictions of bone density across different anatomical locations. The predicted bone density values obtained from the models are then compared with the DXA data measured for each participant, allowing for evaluation and validation of the prediction accuracy. The overall goal is to assess the performance of the optical bone densitometer and its ability to accurately predict bone density compared to the reference DXA measurements. In addition to the bone density prediction models, the study also explored the use of class activation mapping (CAM) to gain insights into the decision-making process within the network models. CAM is a technique that allows visualization of the regions of an input image that contribute the most to the network's prediction. It helps to understand which parts of the image are important in the model's decision-making process [22], [23]. By applying CAM to the trained models, the study aimed to identify the specific regions in the input images that the models focused on when making predictions. This analysis can provide valuable insights into the features or patterns that the models deemed significant for bone density estimation. CAM helps researchers and clinicians understand the underlying factors considered by the models, which can further enhance the interpretability and trustworthiness of the predictions made by the optical bone densitometer.

III. RESULTS AND DISCUSSION
In this study, bone density prediction is conducted for a cohort of 57 participants across multiple positions, as illustrated in Figure 5. Each participant contributes 12 sets of data,

**TABLE 1.** Prediction results for all radius and ulna test data.

Subject	Distal Radius			Distal Ulna		
	DXA	Pred.	Error %	DXA	Pred.	Error %
Sub1_L	0.425	0.405	5%	0.268	0.248	7%
Sub2_L	0.41	0.427	4%	0.28	0.301	7%
Sub3_L	0.429	0.422	2%	0.345	0.352	2%
Sub4_L	0.373	0.389	4%	0.284	0.276	3%
Sub1_R	0.35	0.364	4%	0.291	0.304	4%
Sub1_R	0.43	0.403	6%	0.336	0.312	7%
Sub1_R	0.36	0.358	1%	0.21	0.203	3%
Sub1_R	0.296	0.308	4%	0.274	0.286	4%
Subject	**Radius 33%**			**Ulna 33%**		
	DXA	Pred.	Error %	DXA	Pred.	Error %
Sub1_L	0.749	0.777	4%	0.699	0.743	6%
Sub2_L	0.7	0.666	5%	0.993	0.932	6%
Sub3_L	0.709	0.766	8%	0.727	0.766	5%
Sub4_L	0.582	0.63	8%	0.662	0.724	9%
Sub1_R	0.674	0.729	8%	0.66	0.704	7%
Sub1_R	0.765	0.7	8%	0.859	0.789	8%
Sub1_R	0.69	0.725	5%	0.687	0.751	9%
Sub1_R	0.582	0.612	5%	0.724	0.754	4%
Subject	**Total Radius**			**Total Ulna**		
	DXA	Pred.	Error %	DXA	Pred.	Error %
Sub1_L	0.646	0.595	8%	0.551	0.575	4%
Sub2_L	0.553	0.606	10%	0.508	0.543	7%
Sub3_L	0.652	0.687	5%	0.618	0.592	4%
Sub4_L	0.626	0.622	1%	0.574	0.56	2%
Sub1_R	0.51	0.537	5%	0.475	0.503	6%
Sub1_R	0.629	0.585	7%	0.598	0.538	10%
Sub1_R	0.549	0.535	3%	0.446	0.439	2%
Sub1_R	0.411	0.46	12%	0.472	0.5	6%

consisting of measurements taken from both the left and right hand, with two measurements per wavelength. Out of these 12 sets, 90% of the data is allocated for training purposes, while the remaining 10% is reserved for validation. The prediction result for each position shall be analyzed and studied. We also checked the degree of influence of various parameters (age, sex, menopause status, fracture, and bone images) on the bone density predictions by analyzing the gradient method in CAM, we can find which area plays vital roles in the prediction process and understand them separately.

A. RADIUS AND ULNA
Fig. 6 illustrates the different positions, including the Distal Radius (Radius UD), Distal Ulna (Ulna UD), Distal Radius 33% (Radius 33%), Distal Ulna 33% (Ulna 33%) for the right hand, and complete Radius (Total Radius) with complete Ulna (Total Ulna) for the left hand, each marked with distinct colors. To ensure data quality, any incomplete or noisy data points were removed from the dataset. Subsequently, the models were trained using the remaining 31 data points for training purposes, while 4 data points were reserved for testing and evaluation. Table 1 presents the predicted values for the four testing data points obtained from all the radius and ulna models. The average percentage error for the distal radius was approximately 3.75% ± 1.5%, indicating a strong
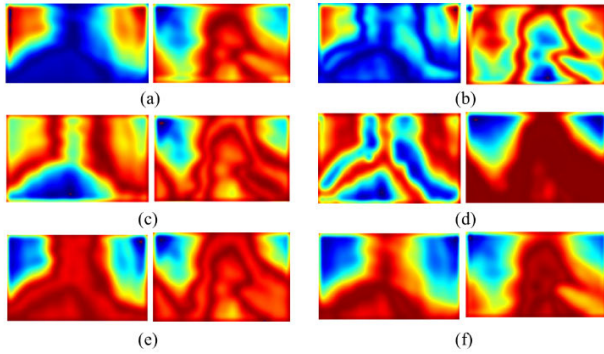
FIGURE 7. Class activation mapping for (a) Distal radius left and distal radius right (b) Distal ulna left and distal ulna right (c) Radius 33% left and radius 33% right (d) Ulna 33%left and ulna 33% right (e) Total radius left and total radius right (f) Total ulna left and total ulna right.

Subject	L1			L2		
	DXA	**Pred.**	**Error %**	**DXA**	**Pred.**	**Error %**
Sub1	1.01	0.891	12%	1.145	1.025	10%
Sub2	0.945	0.937	1%	0.818	0.937	15%
Sub3	0.886	0.916	3%	1.003	1.107	10%
Subject	**L3**			**L4**		
	DXA	**Pred.**	**Error %**	**DXA**	**Pred.**	**Error %**
Sub1	1.01	0.891	12%	1.145	1.025	10%
Sub2	0.945	0.937	1%	0.818	0.937	15%
Sub3	0.886	0.916	3%	1.003	1.107	10%
Subject	**Spine Average**					
	DXA	**Pred.**	**Error %**			
Sub1	0.854	0.954	12%			
Sub2	1.01	1.07	6%			
Sub3	0.989	1.04	5%			

agreement with the DXA measurement data. This particular model demonstrated the best performance compared to the other models. On the other hand, the distal ulna model yielded an average percentage error of 4.6% ± 2% which also highly fits the DXA data. The slightly higher error percentage in comparison to the distal radius may be due to the indirect measurement area of the ulna. The CAM of the radius and ulna models for both left and right is shown in Fig. 7. By analyzing the CAM of the distal radius, we can observe that the prediction model captures the positions around the distal radius for the right hand. It focuses on the area where there are significant changes in light intensity at the edge, indicating its relevance in predicting the BMD for the right radius. Conversely, for the left hand, the model places attention on both the areas of the distal radius and ulna to predict the BMD of the left radius. This suggests that the model considers multiple regions in the left hand to make accurate predictions of bone density.

In the case of the right ulna, we observed that the model also emphasizes the light intensity at the edge of the radius. This could be attributed to the overlapping nature of the radius and ulna at the edge, leading to inconsistent focus in the Class Activation Mapping (CAM) results. On the other hand, for the distal ulna of the left hand, the model exhibits a similar focus to that of the left radius, but with more emphasis on the ulna side. This indicates that the model considers both the radius and ulna regions in the left hand for predicting bone density, with a slightly higher emphasis on the ulna. The prediction results for the distal radius 33% and distal ulna 33% positions exhibited an average percentage error of 6.38%±2% and 6.75%±2% respectively, which indicates a relatively higher error compared to the distal radius and ulna positions. The CAM analysis revealed certain inconsistencies in key areas. For instance, the CAM of the right Radius 33% model resembled the CAM model of the distal radius, while the CAM of the left hand was similar to that of the distal ulna but with a greater focus on the middle bone area. Similarly, the total radius and total ulna models also demonstrated an average percentage error similar to that of the 33% radius

and 33% ulna, with values of 6.88%±3% and 5.13%±1.5% respectively. The CAM models for these positions also exhibited similar inconsistencies. Despite these inconsistencies, the CAM analysis showed comparable focus when predicting the bone mineral density (BMD) of the right hand. The Mean Average Percentage Error (MAPE) of the radius and ulna models can be visualized in Fig. 10.

B. SPINE (L1, L2, L3 AND L4)
In Fig 6, the spine positions L1, L2, L3, and L4 are denoted by the colors red, green, blue, and purple, respectively. To analyze the bone mineral density (BMD) of the spine at these positions (L1-L4), we take into consideration Wolff's Law. According to Wolff's Law, bones subjected to higher pressure or load tend to experience increased growth, densification, and hardening, resulting in greater tolerance to stress. Conversely, bones subjected to lower pressure or load may exhibit reduced growth and lower density. Hence, from L1 down to L4, the BMD must increase as we go down. If the BMD measurements obtained from dual-energy X-ray absorptiometry (DXA) do not follow Wolff's Law, indicating an abnormal pattern, those specific BMD values are considered atypical. In such cases, if a participant has two or more abnormal BMD values, the entire dataset associated with that participant is excluded from the study. To assess the adherence to Wolff's Law, we compared the bone density measurements of each subject from L1 to L4, with L4 serving as the reference standard. Any data points that did not conform to Wolff's Law were deemed noncompliant and excluded from model development. Upon analyzing the DXA measurements, the dataset was distributed as follows: L1 - 26 training data and 3 testing data, L2 - 32 training data and 4 testing data, L3 - 18 training data and 3 testing data, and L4 - 29 training data and 4 testing data. The predicted values for the testing data are presented in Table 2. The average percentage errors for L1, L2, L3, and L4 are 5.3% ± 5%, 11.3% ± 8%,
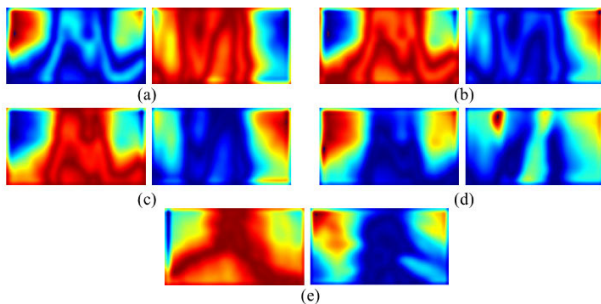
FIGURE 8. Class activation mapping for spine (a) L1 (b) L2 (c) L3 and (d) L4 via left wrist image and Right wrist image (e) The spine average bone density via the left and right hand.

11.67% ± 2%, and 8.50% ± 7%, respectively, as illustrated in Fig. 11(a).

The CAM model of each of the spine positions showed little consistency making it hard to distinguish the decision of the network model as shown in Fig 8.

When we averaged the DXA bone density values of L1-L4 and directly predicted the BMD, we obtained similar average percentage errors. However, the CAM model analysis revealed that the BMD prediction process for the spine in our study heavily relied on the left distal radius image. The CAM visualization (Fig 8(e)) demonstrated the strong correlation between the left distal radius image and the spine BMD prediction. This suggests that the information captured in the left distal radius image played a crucial role in estimating the BMD of the spine.

C. HIP (NECK LEFT, NECK RIGHT, TOTAL LEFT, AND TOTAL RIGHT)

Following Wolff's law, the left femoral neck is expected to have a lower BMD compared to the total left hip (and similarly for the right side). The specific hip positions, including the femoral neck and the total left and right areas, are marked in Fig. 6. The small red box indicates the neck area, while the larger yellow area represents the total left and right hip regions, respectively. Following the same principle as before, if a participant's BMD data from DXA does not adhere to Wolff's law, their data is excluded from the study. After carefully analyzing the BMD data obtained from DXA, the dataset is distributed as follows: Neck left - 27 training data and 3 testing data, Total Left - 27 training data and 3 testing data, Neck right - 28 training data and 3 testing data, and Total right - 28 training data and 3 testing data. The predicted values of the Hip BMD are presented in Table 3. The average percentage error for the Neck left and Total left was approximately 13% ± 5% with a standard deviation of 0.045, while the Neck right and Total right exhibited an average percentage error of about 15% ± 7% and 9% ± 6% respectively, as depicted in Fig. 11(b). Although the error margin is relatively high, a notable observation from this hip bone study is the significant influence of the distal radius images of the opposite hand on the prediction of the neck left
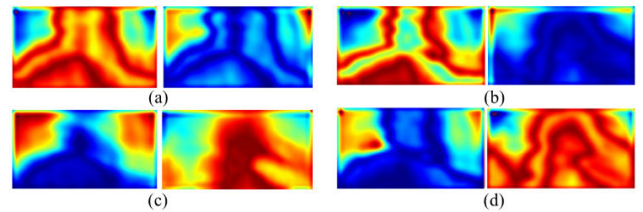
FIGURE 9. Class activation mapping for (a) Hip Neck right (b) Hip total right (c) Hip neck left (d) Hip total left via left wrist image and right wrist image.
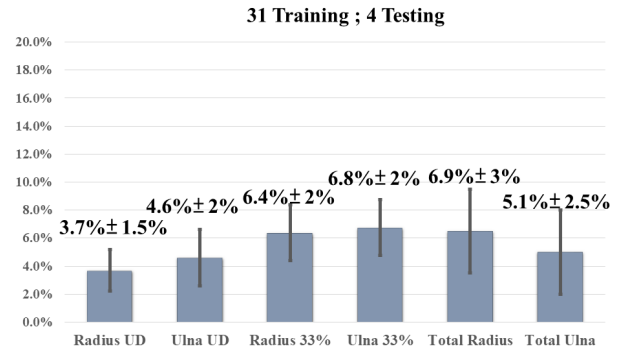
FIGURE 10. Mean average percentage error at all radius regions \.

**TABLE 3.** Prediction results for all spine test data.

Subject	Neck Left			Total Left		
	DXA	Pred.	Error %	DXA	Pred.	Error %
Sub1	0.618	0.728	18%	0.722	0.842	17%
Sub2	0.885	0.742	16%	1.019	0.86	16%
Sub3	0.698	0.729	4%	0.78	0.833	7%
Subject	**Neck Right**			**Total Right**		
	DXA	Pred.	Error %	DXA	Pred.	Error %
Sub1	0.857	0.815	5%	0.906	0.831	8%
Sub2	0.728	0.809	11%	0.824	0.808	2%
Sub3	0.981	0.805	18%	1.053	0.865	18%

and total left bone density, and similarly, the left distal radius wrist images heavily impact the prediction of bone density on the right side, as demonstrated in Fig. 9.

These outcomes suggest a strong relationship between the bone density of the right radius and the left hip, and vice versa for the right side.

D. SIGNIFICANCE OF OTHER FEATURES

We have successfully developed a cost-effective device utilizing a near-infrared imaging system to screen and predict bone density in different positions, including the Left and Right wrist (Radius, Radius 33%, Total Radius, Ulna, Ulna 33%, Total Ulna), Left and Right Hip (Neck and Total Neck), and Spine (L1, L2, L3, L4, and Spine average). Through comprehensive analysis of the prediction results across all positions, it is evident that the local bone density prediction model for the Radius and Ulna exhibits higher accuracy compared to
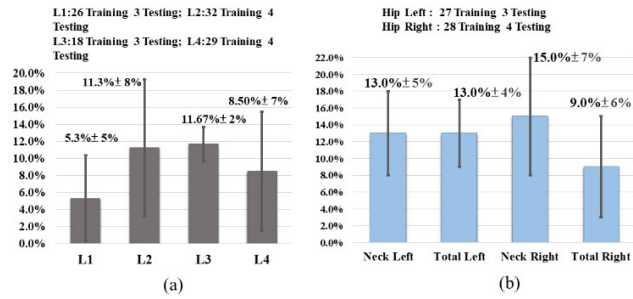
FIGURE 11. Mean average percentage error at all (a) Spine and (b) Hip regions.

other models. This highlights the efficacy of our approach in accurately assessing bone density using the near-infrared imaging system. The CAM gradient study for the Radius and Ulna was conducted on a 65-year-old woman with menopause and no history of fractures. The study revealed that the bone density network predominantly extracted information from the distal radius image, indicating that the bone information provided by the OBD image was adequate for predicting Radius and Ulna bone density. Among the physiological data, age, sex, and menopause status of the participant were found to significantly influence the prediction, with menopause status contributing the most information among the three factors. Despite the irregular distribution observed in the CAM analysis for the spine, the gradient data revealed that both the left and right hands provided valuable information for predicting spine bone density. The CAM gradient study for the spine was conducted on a 60-year-old woman with menopause and a history of fractures. In this study, the influence of menopause was found to be more prominent, while the impact of fractured bone information was further amplified. The age and sex of the participants still demonstrated a significant influence on the prediction results. Regarding the prediction of hip bone density, it was initially anticipated that the correlation between the OBD images and the hip bone would be relatively consistent. However, the study revealed that the neck left and total left hip bone density predictions were heavily influenced by the right wrist images, while the right side exhibited a strong dependence on the left wrist images. This investigation involved a 65-year-old woman with menopause and no history of fractures. The participant's age was found to have the most significant impact on the physiological data, while the influence of menopause was also prominent in this study. It is important to note that further research with a larger dataset is necessary to draw conclusive findings regarding the spine and hip bone density predictions based on these observations.

While our results showcase the effectiveness of the chosen hardware in achieving our study objectives, it is pertinent to note that certain aspects of our findings may have implications for the feasibility of alternative equipment. For instance, variations in image quality or accuracy may be observed when different hardware configurations are considered.

IV. CONCLUSION

In this research, we have successfully developed a low-cost OBD system based on near-infrared imaging combined with deep learning, which is non-invasive, and cost-effective with localized measurements. This system offers a rapid and effective method for screening the bone density of individuals. It is worth noting that no adverse side effects were observed during the study. In terms of accuracy, the measurements of local radius and ulna bone density exhibited promising results compared to DXA, with an error margin below 10%. These findings highlight the potential of our OBD system as a reliable alternative for bone density assessment. Furthermore, the neural network visualization provided valuable insights into the contributions of each feature in the prediction model. The study emphasizes the distal radius image's crucial role in predicting Radius and Ulna bone density, showcasing the effectiveness of the OBD image for this purpose. Additionally, an analysis of physiological factors—age, sex, and menopause status—reveals their significant impact on bone density predictions. Notably, menopause status contributes the most information among these factors. To enhance clinical transparency, the study includes sensitivity analysis and clinical validation, ensuring alignment with established clinical reasoning. This comprehensive approach underscores the model's transparency, robustness, and relevance in predicting bone density across diverse physiological contexts.

Although the error margin for hip and spine measurements was relatively high, falling within 20% of the true value, it is important to note that bone density of the spine and hip is widely used as a criterion in clinical settings. Therefore, achieving an error within 20% is still not sufficient, but it does show potential for improvement. In the future, enhancing prediction accuracy can be achieved by gathering a larger dataset with more participants. We aim to establish a comprehensive database specific to the optical bone density detection system. This will enable simpler comparisons of T-score values for individuals, rather than solely relying on absolute bone density measurements. Such a database would provide individuals with clearer insights into their bone density status and assist in monitoring their bone health. In comparison to traditional Dual-Energy X-ray Absorptiometry (DXA), our intelligent optical bone density system exhibits several noteworthy advantages. Firstly, the real-time capability of our system allows for immediate results, addressing a significant drawback of DXA, which often involves time-consuming processes and post-assessment analysis. Additionally, the non-invasiveness of our system eliminates concerns associated with ionizing radiation exposure, a key limitation of DXA. The cost-effectiveness further enhances the appeal of our system, making it more accessible for routine clinical assessments.

Furthermore, the portability of our system stands in contrast to the stationary nature of DXA machines, offering a more flexible and adaptable solution for bone density evaluations. When compared to other non-invasive techniques like

Quantitative Ultrasound (QUS) and Dual-Photon Absorptiometry (DPA), our system maintains similar advantages, emphasizing real-time capability, non-invasiveness, cost-effectiveness, and portability, while providing high-quality imaging and increased accessibility. This integration of technological advantages with practical clinical implications exemplifies the translational potential of our innovation.

Regarding the hardware aspect, it was observed that prolonged operation of the device led to heating issues, primarily due to the high output power of the employed LEDs. To address this, integrating a heat dissipation module could be a beneficial improvement, ensuring both subject comfort and device functionality. Additionally, in the current system, LED control is performed manually, requiring manual intervention for turning on/off and capturing the required images. Automation of the LED control circuit, enabling automated on/off operations and image capture, would be a valuable intervention in future iterations of the system. Overall, Intelligent Optical Bone Densitometry presents a highly promising method for accurately and efficiently assessing bone density, thereby establishing itself as a valuable tool in the realm of bone health assessment and management. Our study in Intelligent Optical Bone Densitometry was conducted with a meticulously chosen set of hardware components, contributing to the precision and reliability of our results. Reflecting on our findings, it is crucial to explore the feasibility of employing alternative equipment to enrich the adaptability and generalizability of our methodology. This exploration involves considering LEDs with varying wavelengths, particularly within the range of 700nm to 1000nm, which introduces intriguing possibilities. Such an investigation has the potential to provide valuable insights into improving the light source, thereby enhancing the quality of near-infrared images. Similarly, delving into alternative small industrial CMOS cameras and lenses emerges as a pivotal avenue for advancing the field of intelligent bone density assessment. Despite leveraging the UI-1250LE-M-GL model by German Imaging Development Systems, future researchers may find value in assessing cameras from diverse manufacturers. Conducting a comparative analysis is essential to grasp the nuanced impact of different imaging devices on the quality of near-infrared images, contributing significantly to the evolution of the field. However, while cost-effective alternatives may present themselves, researchers should be cautious of potential compromises in functionality. It is equally crucial to consider the long-term sustainability and support for chosen hardware configurations, ensuring the reliability and longevity of the adopted systems. In navigating these considerations, researchers must balance the allure of cost-effectiveness with the imperative of maintaining optimal functionality over the long term.

In our research, which concentrated on short-term evaluations of bone density using the near-infrared method, we acknowledged a limitation in our ability to assess the long-term reliability of the method and the fact that we did not include T-score calculations in our study. To address these shortcomings, we are committed to future research endeavors, specifically follow-up studies that involve continuous monitoring of participants. These follow-up studies will not only assess bone density but also incorporate T-score calculations. The goal is to gain a more thorough understanding of how the method performs over an extended period. This commitment contributes to both scientific knowledge and practical applications, particularly in clinical settings where consistent measurements of bone density and T-scores are needed over prolonged durations.

Our study addresses a critical need for accessible bone density assessment tools. Traditional methods such as dual X-ray absorptiometry (DXA) can be expensive, time-consuming, and require specialized equipment and trained professionals. In contrast, our developed system offers ease of operation, real-time bone density prediction, and high accuracy, making it more accessible and practical for a wider population. Overall, the significance of the results lies in the potential impact on bone health management, early detection of bone disorders, and the advancement of non-invasive, cost-effective diagnostic approaches. It contributes to the field of bone health assessment, optics, biomedical systems, image processing, and artificial intelligence, offering valuable insights and potential applications for researchers, clinicians, and individuals concerned about their bone health.

REFERENCES

[1] *Prevention and Management of Osteoporosis*, World Health Org., Geneva, Switzerland, vol. 921, 2003, pp. 1–164.

[2] C. Cooper and S. Ferrari, "IOF compendium of osteoporosis," Int. Osteoporosis Found. (IOF), Nyon, Switzerland, Tech. Rep. 893 (2nd Edition), 2019.

[3] M. P. Ettinger, "Aging bone and osteoporosis: Strategies for preventing fractures in the elderly," *Arch. Internal Med.*, vol. 163, pp. 2237–2246, Oct. 2003.

[4] J. A. Kanis and J. A. Kanis, "Assessment of fracture risk and its application to screening for postmenopausal osteoporosis: Synopsis of a WHO report," *Osteoporosis Int.*, vol. 4, no. 6, pp. 368–381, Nov. 1994.

[5] S. Guerri et al., "Quantitative imaging techniques for the assessment of osteoporosis and sarcopenia," *Quant. Imag. Med. Surgery*, vol. 8, no. 1, pp. 60–85, Feb. 2018.

[6] *ISCD Official Positions-Adult*, International Society for Clinical Densitometry, Middletown, CT, USA, 2019.

[7] A. B. Gandhi and A. K. R. Shukla, "Evaluation of BMD of women above 40 years of age," *J. Obstet. Gynecol. India*, vol. 55, pp. 265–267, Jul. 2005.

[8] W. W. Peppler and R. B. Mazess, "Total body bone mineral and lean body mass by dual-photon absorptiometry," *Calcified Tissue Int.*, vol. 33, no. 1, pp. 353–359, Dec. 1981.

[9] H. K. Genant, "Quantitative computed tomography of vertebral spongiosa: A sensitive method for detecting early bone loss after oophorectomy," *Ann. Internal Med.*, vol. 97, no. 5, pp. 699–705, Nov. 1982.

[10] S. Boutroy, M. L. Bouxsein, F. Munoz, and P. D. Delmas, "In Vivo assessment of trabecular bone microarchitecture by high-resolution peripheral quantitative computed tomography," *J. Clin. Endocrinology Metabolism*, vol. 90, no. 12, pp. 6508–6515, Dec. 2005.

[11] D. C. Bauer, "Broadband ultrasound attenuation predicts fractures strongly and independently of densitometry in older women. a prospective study. Study of osteoporotic fractures research group," *Arch. Internal Med.*, vol. 157, pp. 629–634, Mar. 1997.

[12] G. M. Blake and I. Fogelman, "Technical principles of dual energy X-ray absorptiometry," *Seminars Nucl. Med.*, vol. 27, no. 3, pp. 210–228, Jul. 1997.

[13] J. T. Schousboe, J. A. Shepherd, J. P. Bilezikian, and S. Baim, "Executive summary of the 2013 international society for clinical densitometry position development conference on bone densitometry," *J. Clin. Densitometry*, vol. 16, no. 4, pp. 455–466, Oct. 2013.

[14] K. Engelke et al., "Clinical use of quantitative computed tomography and peripheral quantitative computed tomography in the management of osteoporosis in adults: The 2007 ISCD official positions," *J. Clin. Densitometry*, vol. 11, no. 1, pp. 123–162, Jan. 2008.

[15] M. L. Frost, G. M. Blake, and I. Fogelman, "Does the combination of quantitative ultrasound and dual-energy X-ray absorptiometry improve fracture discrimination?" *Osteoporosis Int.*, vol. 12, no. 6, pp. 471–477, Jun. 2001.

[16] D. C. Sordillo, L. A. Sordillo, P. P. Sordillo, L. Shi, and R. R. Alfano, "Short wavelength infrared optical windows for evaluation of benign and malignant tissues," *J. Biomed. Opt.*, vol. 22, no. 4, Apr. 2017, Art. no. 045002.

[17] V. V. Tuchin, "Tissue optics," in *Society of Photo-Optical Instrumentation Engineers*. Bellingham, WA, USA: SPIE, 2015.

[18] A. Takeuchi et al., "A new method of bone tissue measurement based upon light scattering," *J. Bone Mineral Res.*, vol. 12, no. 2, pp. 261–266, Feb. 1997.

[19] C. Chung, Y. Chen, T. Leu, and C. Sun, "Near-infrared bone densitometry: A feasibility study on distal radius measurement," *J. Biophotonics*, vol. 11, no. 7, Jul. 2018, Art. no. e201700342.

[20] M. M. Ahsan, S. A. Luna, and Z. Siddique, "Machine-learning-based disease diagnosis: A comprehensive review," *Healthcare*, vol. 10, no. 3, p. 541, Mar. 2022.

[21] O. Ronneberger, P. Fischer, and T. Brox, "U-net: Convolutional networks for biomedical image segmentation," in *Proc. Int. Conf. Med. Image Comput. Comput.-Assist. Intervent.* Cham, Switzerland: Springer, 2015, pp. 234–241.

[22] B. Zhou, A. Khosla, A. Lapedriza, A. Oliva, and A. Torralba, "Learning deep features for discriminative localization," in *Proc. IEEE Conf. Comput. Vis. Pattern Recognit. (CVPR)*, Jun. 2016, pp. 2921–2929.

[23] R. R. Selvaraju, M. Cogswell, A. Das, R. Vedantam, D. Parikh, and D. Batra, "Grad-CAM: Visual explanations from deep networks via gradient-based localization," in *Proc. IEEE Int. Conf. Comput. Vis. (ICCV)*, Oct. 2017, pp. 618–626.

• • •